

Anatomically Guided Latent Diffusion for Brain MRI Progression Modeling

Cheng Wan, Bahram Jafrahesteh, Ehsan Adeli, Miaomiao Zhang, and Qingyu Zhao

arXiv:2601.14584v1 [cs.CV] 21 Jan 2026

Abstract— Accurately modeling longitudinal brain MRI progression is crucial for understanding neurodegenerative diseases and predicting individualized structural changes. Existing state-of-the-art approaches, such as Brain Latent Progression (BrLP), often use multi-stage training pipelines with auxiliary conditioning modules but suffer from architectural complexity, suboptimal use of conditional clinical covariates, and limited guarantees of anatomical consistency. We propose Anatomically Guided Latent Diffusion Model (AG-LDM), a segmentation-guided framework that enforces anatomically consistent progression while substantially simplifying the training pipeline. AG-LDM conditions latent diffusion by directly fusing baseline anatomy, noisy follow-up states, and clinical covariates at the input level, a strategy that avoids auxiliary control networks by learning a unified, end-to-end model that represents both anatomy and progression. A lightweight 3D tissue segmentation model (WarpSeg) provides explicit anatomical supervision during both autoencoder fine-tuning and diffusion model training, ensuring consistent brain tissue boundaries and morphometric fidelity. Experiments on 31,713 ADNI longitudinal pairs and zero-shot evaluation on OASIS-3 demonstrate that AG-LDM matches or surpasses more complex diffusion models, achieving state-of-the-art image quality and 15-20% reduction in volumetric errors in generated images. AG-LDM also exhibits markedly stronger utilization of temporal and clinical covariates (up to 31.5x higher sensitivity than BrLP) and generates biologically plausible counterfactual trajectories, accurately capturing hallmarks of Alzheimer’s progression such as limbic atrophy and ventricular expansion. These results highlight AG-LDM as an efficient, anatomically grounded framework for reliable brain MRI progression modeling.

Index Terms— Brain MRI, diffusion models, disease progression, latent space, medical imaging, segmentation supervision

I. INTRODUCTION

The human brain undergoes profound, heterogeneous changes across the lifespan, with trajectories shaped by sociodemographic factors, life experiences, and diseases such as Alzheimer’s disease (AD). The ability to model and predict individual-level structural brain changes is crucial for understanding how development and aging are influenced by external factors, and for enabling early diagnosis, treatment planning, and monitoring disease progression [1], [2]. While traditional statistical approaches [3], [4] provide population-level insights, they fail to capture the complex spatiotemporal patterns characterizing individual disease trajectories. To address this, deep generative models have emerged as a powerful paradigm to simulate future brain MRIs from past observations. Early approaches based on Generative Adversarial Networks (GANs) [5], [6] and Variational Autoencoders (VAEs) [7] often suffer from training instability or over-smoothing. More recently, diffusion models [1], [8], [9] have established a new standard, offering superior stability and high-quality generation.

Among recent developments, Brain Latent Progression (BrLP) [1] represents the current state-of-the-art for brain MRI progression modeling. BrLP combines latent diffusion models with a ControlNet module and an auxiliary disease progression module, achieving impressive performance across multiple datasets. However, BrLP’s success comes at the cost of architectural complexity, requiring a three-stage training pipeline, in which the ControlNet module must learn to condition the diffusion process on baseline images through cross-attention mechanisms. The auxiliary disease progression module relies on having volume trajectories of five *a-priori* selected brain regions specific to AD. This design increases computational overhead, restricts its applicability to one disease, and overlooks changes in other important brain regions.

Despite significant progress of BrLP in brain MRI progression modeling, several key issues remain unprobed. Traditional approaches train generative models by optimizing voxel-level intensity reconstruction and evaluate models by image-quality metrics. As synthetic MRIs achieve near-perfect visual quality, subtle anatomical inaccuracies become harder to detect by human experts or existing metrics [10], [11], necessitating training protocols that explicitly maintain accurate morphometric properties in regions and tissue types that are essential for clinical interpretation. Second, effectively incorporating conditional information remains challenging. While models

This work was supported in part by the National Artificial Intelligence Research Resource (NAIRR) Pilot Grant NAIIRR250120.

C. Wan is with the Department of Electrical and Computer Engineering, Cornell University, Ithaca, NY, USA, and also with the Department of Radiology, Weill Cornell Medicine, New York, NY, USA (e-mail: cw2222@cornell.edu).

B. Jafrahesteh and Q. Zhao are with the Department of Radiology, Weill Cornell Medicine, New York, NY, USA (e-mail: baj4003@med.cornell.edu; qiz4006@med.cornell.edu).

E. Adeli is with the Department of Psychiatry and Behavioral Sciences, Stanford University, Stanford, CA, USA (e-mail: eadeli@stanford.edu).

M. Zhang is with the Department of Electrical and Computer Engineering, University of Virginia, Charlottesville, VA, USA (e-mail: mz8rr@virginia.edu).

can be conditioned on various clinical covariates (age, sex, diagnosis), ensuring that these conditions meaningfully influence the generation process is non-trivial. Multi-stage architectures with indirect conditioning mechanisms (e.g., through cross-attention or separate control modules) may not fully preserve individual-specific characteristics or leverage temporal information effectively, as conditioning signals must pass through multiple transformation stages during synthesis.

We propose Anatomically Guided Latent Diffusion Model (AG-LDM), a simplified framework for brain MRI progression modeling that addresses these challenges. Our approach combines a streamlined two-stage architecture with explicit anatomical supervision through segmentation guidance. Conditioned on a baseline image and clinical covariates, AG-LDM can generate a future MRI at a given age and clinical diagnosis while enforcing consistent tissue boundaries. AG-LDM achieves state-of-the-art performance while maintaining architectural simplicity and computational efficiency. Our key contributions are threefold:

1) Unified Progression Modeling: Instead of employing auxiliary control networks that inject conditioning as corrective guidance, AG-LDM treats baseline anatomy and clinical covariates as co-equal latent state variables fused directly into the backbone. This design models disease evolution as a unified conditional transition process, enabling stable end-to-end training without the need for multi-stage optimization or guidance-strength tuning.

2) Segmentation-Guided Training: We integrate a lightweight 3D brain tissue segmentation model (WarpSeg) to provide anatomical supervision during both autoencoder fine-tuning and diffusion model training. By embedding baseline anatomy and segmentation directly into the latent diffusion trajectory, this approach allows the model to learn temporally coherent anatomical progression rather than relying on static structural guidance.

3) Comprehensive Evaluation: Extensive experiments on two longitudinal brain MRI datasets demonstrate that AG-LDM achieves comparable or superior image quality and anatomical precision compared to state-of-the-art generative models. Our method reduces volumetric errors by 15-20% in key anatomical regions and maintains strong generalization to unseen external datasets. Results also indicate that AG-LDM can better leverage conditional information in the generation process (e.g., 31.5 \times greater sensitivity to age compared to baseline models). Counterfactual analysis reveals that AG-LDM correctly captures disease-specific progression patterns (e.g., limbic atrophy and ventricular expansion in AD).

II. RELATED WORK

A. Diffusion Models in Medical Imaging

Diffusion models have emerged as a powerful paradigm for high-quality image generation, offering superior training stability compared to GANs and better sample quality than VAEs. The foundational Denoising Diffusion Probabilistic Model (DDPM) [12] introduced a principled approach to generative modeling through iterative denoising. Given a data sample \mathbf{z}_0 , DDPM defines a forward Markov process $q(\mathbf{z}_t|\mathbf{z}_0) =$

$\mathcal{N}(\mathbf{z}_t; \sqrt{\bar{\alpha}_t}\mathbf{z}_0, (1 - \bar{\alpha}_t)\mathbf{I})$ that progressively adds Gaussian noise over T timesteps, where $\{\alpha_t\}_{t=1}^T$ is a predefined noise schedule with $\bar{\alpha}_t = \prod_{i=1}^t \alpha_i$. This allows efficient sampling of noisy versions $\mathbf{z}_t = \sqrt{\bar{\alpha}_t}\mathbf{z}_0 + \sqrt{1 - \bar{\alpha}_t}\epsilon$ with $\epsilon \sim \mathcal{N}(0, \mathbf{I})$. The model learns to reverse this process via a Markov chain $p_\theta(\mathbf{z}_{t-1}|\mathbf{z}_t) = \mathcal{N}(\mathbf{z}_{t-1}; \mu_\theta(\mathbf{z}_t, t), \Sigma_\theta(\mathbf{z}_t, t))$, where the mean μ_θ and variance Σ_θ are parameterized by a neural network. In practice, the network predicts the noise $\epsilon_\theta(\mathbf{z}_t, t)$, and the denoised mean is computed as:

$$\mu_\theta(\mathbf{z}_t, t) = \frac{1}{\sqrt{\alpha_t}} \left(\mathbf{z}_t - \frac{1 - \alpha_t}{\sqrt{1 - \bar{\alpha}_t}} \epsilon_\theta(\mathbf{z}_t, t) \right). \quad (1)$$

This reverse process enables image generation from pure Gaussian noise through iterative denoising.

Building upon DDPM, Latent Diffusion Models (LDM) [13] operate in a compressed latent space to significantly improve computational efficiency while maintaining high generation quality, often leveraging deterministic sampling strategies [14]. In the medical domain, such frameworks have demonstrated promising results for brain image synthesis [15] and disease progression modeling.

B. Brain MRI Generative Models

Deep generative models have been widely explored for brain MRI synthesis. These methods can be categorized based on their generation objective: unconditional/conditional synthesis of new subjects, and longitudinal progression modeling. In the first category, the methods aim to generate high-quality MRIs from noise, often conditioned on metadata or clinical variables. Prior to diffusion models, GAN-based approaches like α -WGAN [16] and CCE-GAN [17] are widely explored but often suffered from unstable training or mode collapse. The use of DDPM resolves this issue, but a direct training of diffusion models in the 3D voxel space, such as performed by 3D-DDPM [18], incurs higher computational costs. In contrast, LDM [15] operates in a compressed latent space, significantly improving computational efficiency. Another way to address memory constraints is to generate volumes via a slice-by-slice approach, such as MedGen3D [19], albeit with potential compromises in global 3D consistency. Building on these, BrainSynth [10] demonstrates high-quality synthesis through vector quantization and masked diffusion. Other approaches have explored conditional diffusion for slice-wise synthesis [20] or integrated physical constraints into latent diffusion models [21] to enhance the plausibility of multimodal synthesis. The synthetic MRIs generated by these models are often used for data augmentation in downstream tasks but rarely used for progression modeling.

To perform progression modeling, generative models have to simulate future MRIs conditioned on past data. To do so, 3D autoregressive diffusion [8] and 2D slice-based diffusion models have been used for longitudinal generation. Other architectures have also been explored; for instance, He et al. [7] propose a VAE-based prediction framework, NeuroAR [22] utilize autoregressive transformers to model subject-specific brain aging trajectories, and Xia et al. [6] utilize GANs to simulate aging without longitudinal data. Among biologically

constrained approaches, 4D-DaniNet [5] simulates progression using adversarial learning, while CounterSynth [23] employs a deformation-based strategy to warp the baseline scan to a target state. In contrast, recent diffusion approaches achieve counterfactual synthesis through latent space manipulations, such as cycle consistency [24] or latent drifting [25]. Lastly, BrLP [1] combines latent diffusion with ControlNet and an auxiliary disease progression model to achieve state-of-the-art performance. However, the complex model architecture and the need for selecting disease-specific brain regions for auxiliary training might limit its use in broader applications.

C. Anatomical Consistency in Medical Image Generation

Ensuring anatomical consistency in generated medical images is crucial for clinical applications. Recent work has shown that conventional image-level metrics such as FID, MS-SSIM, and MMD, while useful for assessing perceptual quality, lack sensitivity to crucial morphometric fidelity [11]. The WASABI (Wasserstein-Based Anatomical Brain Index) metric addresses this gap by explicitly measuring morphometric plausibility through segmentation-derived volumetric measures and multivariate Wasserstein distance. This work demonstrated that synthetic MRIs achieving near-perfect visual quality may still exhibit subtle anatomical inaccuracies that are difficult to detect by human experts or existing metrics, necessitating evaluation protocols that explicitly assess whether generated images reflect true brain anatomy. Beyond evaluation, ensuring anatomical plausibility during training remains challenging. One promising direction is deformation-based synthesis [26]–[28]. For example, MorphLDM [26] generates novel images by applying synthesized deformation fields to a brain template to ensure morphological plausibility. However, these methods assume that the generated images share an identical topological structure with a given template, up to diffeomorphism, which is an overly restricted assumption.

The use of segmentation-guided training has shown particular promise in brain imaging applications. For instance, BrainSPADE [29] uses semantic masks as conditional inputs to control the layout and generate high-quality pathological brains. While effective for label-to-image synthesis where the target anatomy is predefined, such approaches inherently rely on the availability of ground-truth segmentation maps during inference, which restricts their direct applicability to disease progression modeling where the future anatomical state is unknown. To address this, our work employs a lightweight segmentation teacher (WarpSeg) to provide anatomical supervision via loss functions rather than conditional inputs, enabling explicit enforcement of tissue boundary consistency during the progression prediction.

III. METHODS

A. Overview and Formulation

We design AG-LDM as a two-stage framework for longitudinal brain MRI progression. Formally, let $\mathcal{X} \subset \mathbb{R}^{H \times W \times D}$ denote the space of 3D T1-weighted brain MRI volumes. For a subject, we observe a baseline scan $\mathbf{x}^{(A)} \in \mathcal{X}$ acquired at age a^A and a follow-up scan $\mathbf{x}^{(B)} \in \mathcal{X}$ at age

$a^B > a^A$. Associated with each scan is a set of clinical covariates $\mathbf{c} = \{a^{(A)}, a^{(B)}, \text{sex}, d^{(A)}, d^{(B)}\}$, where $d^{(A)}$ and $d^{(B)}$ represent the categorical diagnostic status at baseline and follow-up, respectively. Our objective is to learn a conditional generative model $p_\theta(\mathbf{x}^{(B)} | \mathbf{x}^{(A)}, \mathbf{c})$ that can synthesize anatomically plausible follow-up scans given baseline observations and clinical context. To achieve this while ensuring computational efficiency and stable training, we adopt a latent diffusion framework [13] operating in a compressed latent space $\mathcal{Z} \subset \mathbb{R}^{3 \times H' \times W' \times D'}$. The pipeline comprises two stages: (i) learning an autoencoder to map between a 3D scan and its latent representation, and (ii) learning a conditional latent diffusion model to generate the latent of the follow-up scan. Figure 1 illustrates the complete pipeline.

B. Baseline Pre-trained Variational Autoencoder

To learn a compact latent representation that preserves both low-level image fidelity and high-level anatomical structure, we adopt the 3D variational autoencoder designed in [15] and initialize its parameters from their publicly available pre-trained model.

Specifically, the 3D variational autoencoder has an encoder $\mathcal{E} : \mathcal{X} \rightarrow \mathcal{Z}$ and a decoder $\mathcal{D} : \mathcal{Z} \rightarrow \mathcal{X}$. The encoder maps an input volume \mathbf{x} to a latent representation $\mathbf{z} = \mathcal{E}(\mathbf{x}) = \mu(\mathbf{x}) + \sigma(\mathbf{x}) \odot \epsilon$, where $\epsilon \sim \mathcal{N}(0, \mathbf{I})$ and functions $\mu(\cdot)$ and $\sigma(\cdot)$ are parameterized by the encoder. The latent dimension is 3 channels at spatial resolution (H', W', D') . The decoder then reconstructs the input from the latent.

This autoencoder has been pre-trained on a large-scale brain MRI dataset [15] to minimize a composite loss that balances reconstruction fidelity, latent regularization, adversarial realism, perceptual quality, and feature-level consistency. The baseline autoencoder objective is:

$$\begin{aligned} \mathcal{L}_{\text{AE}} = \mathbb{E}_{\mathbf{x} \sim p_{\text{data}}} & \left[\underbrace{\|\mathbf{x} - \hat{\mathbf{x}}\|_1}_{\text{reconstruction}} + \underbrace{\beta_{\text{KL}} \cdot \text{KL}(q_\phi(\mathbf{z}|\mathbf{x}) \| p(\mathbf{z}))}_{\text{KL regularization}} \right. \\ & + \underbrace{\lambda_{\text{perc}} \cdot \mathcal{L}_{\text{perc}}(\mathbf{x}, \hat{\mathbf{x}})}_{\text{perceptual loss}} + \underbrace{\lambda_{\text{adv}} \cdot \mathcal{L}_{\text{adv}}(\hat{\mathbf{x}})}_{\text{adversarial loss}} + \underbrace{\lambda_{\text{fm}} \cdot \mathcal{L}_{\text{fm}}(\mathbf{x}, \hat{\mathbf{x}})}_{\text{feature matching}} \left. \right], \end{aligned} \quad (2)$$

where $\hat{\mathbf{x}} = \mathcal{D}(\mathcal{E}(\mathbf{x}))$ is the reconstruction. The perceptual loss uses a pre-trained 3D feature extractor capturing high-level semantic similarity. The adversarial loss uses a patch-based discriminator \mathcal{D}_{adv} with spectral normalization to encourage realistic local texture. The feature matching loss \mathcal{L}_{fm} stabilizes adversarial training by encouraging intermediate discriminator feature similarity between real and reconstructed images:

$$\mathcal{L}_{\text{fm}}(\mathbf{x}, \hat{\mathbf{x}}) = \frac{1}{L} \sum_{l=1}^L \|\mathcal{D}_{\text{adv}}^{(l)}(\mathbf{x}) - \mathcal{D}_{\text{adv}}^{(l)}(\hat{\mathbf{x}})\|_1, \quad (3)$$

where $\{\mathcal{D}_{\text{adv}}^{(l)}\}_{l=1}^L$ denote the L intermediate feature layers of the discriminator, and the discriminator features for real images are computed with gradients disabled.

C. Stage 1: Fine-tuning with Anatomical Supervision

The first stage of our model aims to fine-tune the pre-trained autoencoder on all MRIs in the training data. A critical

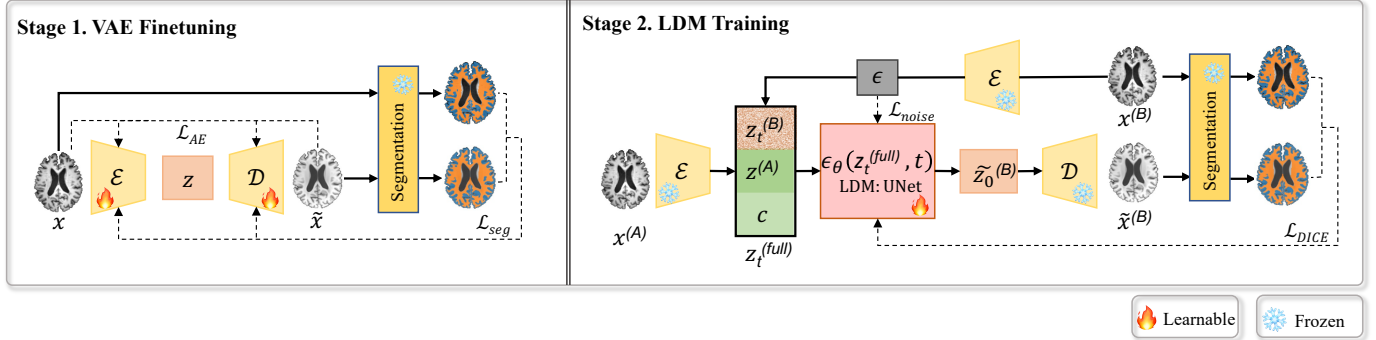


Fig. 1: AG-LDM is a two-stage brain MRI generative model: Stage 1 first fine-tunes a Variational Autoencoder (VAE) to learn latent representations of MRIs, whereas Stage 2 trains a Latent Diffusion Model (LDM) that generates the latent of the future MRI conditioned on the latent of the baseline MRI and other clinical covariates (e.g., sex, age and diagnosis information at time A and time B). In both stages, segmentation guidance is used to ensure the reconstructed MRI has consistent GM and WM tissue segmentation as the ground-truth.

challenge in brain MRI progression modeling is maintaining anatomical consistency while capturing disease-related structural changes. We address this by integrating a lightweight tissue-segmentation teacher into the model such that the reconstructed scan and the input MRI have consistent tissue-segmentation results.

1) *Segmentation Guidance*: To guide VAE fine-tuning, we require a pre-trained segmentation teacher. While tools like SynthSeg [30] and FastSurfer [31] offer robust segmentation, they present significant integration bottlenecks. SynthSeg is implemented in TensorFlow, introducing substantial cross-framework overhead and memory costs within our PyTorch-based pipeline. Conversely, FastSurfer employs a resource-intensive 2D slice-aggregation strategy that results in high latency. Given the necessity for thousands of iterative calls during training, the computational inefficiencies of these tools render them impractical for our end-to-end optimization.

To resolve these challenges, we employ WarpSeg [32], an in-house-trained compact 3D U-Net-based segmentation network $\Phi : \mathcal{X} \rightarrow \mathbb{R}^{6 \times H \times W \times D}$ with 2.1M parameters that enables efficient repeated inference during training. WarpSeg is pre-trained on a large-scale brain segmentation dataset to generate 6-class tissue or region segmentation. In our work, we initially focus on preserving white matter (WM) and gray matter (GM) structures, as these define the fundamental cortical and subcortical boundaries that should remain stable during disease progression. Specifically, for any input image \mathbf{x} , the segmentor output $\mathbf{s} = \Phi(\mathbf{x})$ contains softmax probability maps $s_k \in [0, 1]^{H \times W \times D}$, where $k = 1$ corresponds to the label map for WM and $k = 2$ for GM. For the reconstructed image $\hat{\mathbf{x}} = \mathcal{D}(\mathcal{E}(\mathbf{x}))$, its corresponding segmentation is $\hat{\mathbf{s}} = \Phi(\hat{\mathbf{x}})$. Now we define two complementary losses. First, the soft Dice loss measures region overlap:

$$\mathcal{L}_{\text{dice}}(\mathbf{x}, \hat{\mathbf{x}}) = 1 - \frac{1}{2} \sum_{k \in \{1, 2\}} \frac{2 \langle \mathbf{s}_k, \hat{\mathbf{s}}_k \rangle + \delta}{\|\mathbf{s}_k\|_1 + \|\hat{\mathbf{s}}_k\|_1 + \delta}, \quad (4)$$

where $\langle \cdot, \cdot \rangle$ denotes the inner product over all spatial locations, $\|\cdot\|_1$ denotes the L_1 norm, and $\delta = 10^{-7}$ is a small constant for numerical stability. Second, to enforce sharp tissue boundaries,

we define a cross-entropy based boundary loss:

$$\mathcal{L}_{\text{boundary}}(\mathbf{x}, \hat{\mathbf{x}}) = -\frac{1}{2} \sum_{k \in \{1, 2\}} \sum_{i=1}^{HWD} s_{k,i} \log \hat{s}_{k,i}. \quad (5)$$

The complete anatomical supervision for autoencoder fine-tuning combines both terms:

$$\mathcal{L}_{\text{seg}}(\mathbf{x}, \hat{\mathbf{x}}) = \mathcal{L}_{\text{dice}}(\mathbf{x}, \hat{\mathbf{x}}) + \mathcal{L}_{\text{boundary}}(\mathbf{x}, \hat{\mathbf{x}}). \quad (6)$$

With such anatomical supervision, the autoencoder is fine-tuned by augmenting the baseline objective (Eq. 2) with \mathcal{L}_{seg} :

$$\mathcal{L}_{\text{AE-finetune}} = \mathcal{L}_{\text{AE}} + \lambda_{\text{seg}} \cdot \mathcal{L}_{\text{seg}}(\mathbf{x}, \hat{\mathbf{x}}), \quad (7)$$

where λ_{seg} is a hyperparameter.

Note, gradients flow only through the generated image $\hat{\mathbf{x}}$, while the segmentor Φ remains *frozen* during training to provide consistent anatomical supervision without introducing additional trainable parameters. This practice ensures that WM and GM boundaries are faithfully preserved in the learned latent space.

D. Stage 2: Conditional Latent Diffusion Model

The second stage models the conditional distribution of follow-up scans in the learned latent space. Our goal is to generate the latent of the follow-up scan $\mathbf{z}^{(B)}$ conditioned on baseline information $\mathbf{z}^{(A)}$ and clinical covariates \mathbf{c} . Building upon the diffusion framework introduced in Sec. II, we take the follow-up latent $\mathbf{z}_0^{(B)} = \mathcal{E}(\mathbf{x}^{(B)})$ and apply the forward process with noise $\epsilon \sim \mathcal{N}(0, \mathbf{I})$ to sample a noisy version $\mathbf{z}_t^{(B)}$ at any timestep t . The core design philosophy of our approach treats longitudinal progression as a conditional transition within a unified latent space rather than separating the generative prior from the conditioning signal (as in ControlNet-style architectures).

1) *Unified Latent Space Fusion*: To implement this unified conditioning, we construct an augmented input at each diffusion timestep t by combining the noisy follow-up latent $\mathbf{z}_t^{(B)}$, the clean baseline latent $\mathbf{z}^{(A)} = \mathcal{E}(\mathbf{x}^{(A)})$, and spatially broadcast clinical covariates $\mathbf{c} \in \mathbb{R}^{5 \times H' \times W' \times D'}$ (i.e. each spatial

location has an identical 5-channel feature $[a^{(A)}, a^{(B)}, \text{sex}, d^{(A)}, d^{(B)}]$. This results in a 11-channel composite input (3 channels for noisy follow-up, 3 for baseline, 5 for covariates):

$$\mathbf{z}_t^{(\text{full})} = [\mathbf{z}_t^{(B)}, \mathbf{z}^{(A)}, \mathbf{c}] \in \mathbb{R}^{11 \times H' \times W' \times D'}, \quad (8)$$

By constructing this composite input, AG-LDM treats baseline anatomy, noisy follow-up states, and clinical covariates as co-equal latent variables. This allows the network to learn a unified score field that jointly represents anatomy and progression, effectively modeling disease evolution as a conditional transition process without the need for auxiliary control networks or guidance-strength tuning. A noise prediction network $\epsilon_\theta(\mathbf{z}_t^{(\text{full})}, t) : \mathbb{R}^{11 \times H' \times W' \times D' \times \mathbb{N}} \rightarrow \mathcal{Z}$ processes this input to predict the noise component.

The network ϵ_θ is implemented as a 3D U-Net following the architecture of LDM [15] (detailed specifications are provided in Sec. IV). The primary objective minimizes the mean squared error between predicted and true noise ϵ , following standard diffusion model training:

$$\mathcal{L}_{\text{noise}} = \mathbb{E}_{t \sim \mathcal{U}(1, T), \epsilon \sim \mathcal{N}(0, \mathbf{I})} [\|\epsilon - \epsilon_\theta(\mathbf{z}_t^{(\text{full})}, t)\|_2^2]. \quad (9)$$

Finally, the denoised latent $\tilde{\mathbf{z}}_0^{(B)}$ is computed using the reverse process mean function defined in Eq. 1.

2) Segmentation-Guided Training: While the above noise prediction objective ensures accurate diffusion modeling, it does not explicitly enforce anatomical plausibility of the generated images. To address this, we augment the training with periodic anatomical supervision. Specifically, after every f_{seg} iterations, we perform a fast 10-step DDIM denoising [14] from an intermediate noisy state to obtain a denoised latent $\tilde{\mathbf{z}}_0^{(B)}$. We then decode this to image space $\tilde{\mathbf{x}}^{(B)} = \mathcal{D}(\tilde{\mathbf{z}}_0^{(B)})$ to produce a generated follow-up scan, and apply the Dice loss as in Eq. 4 to minimize the difference in tissue segmentation between ground-truth and generated follow-up MRI:

$$\mathcal{L}_{\text{LDM}} = \mathcal{L}_{\text{noise}} + \gamma \cdot \mathcal{L}_{\text{dice}}(\mathbf{x}^{(B)}, \tilde{\mathbf{x}}^{(B)}), \quad (10)$$

where γ is a small weight balancing noise prediction accuracy with anatomical consistency. Note, the segmentor remains frozen to provide consistent anatomical guidance. This dual objective ensures that the learned diffusion model not only accurately models the data distribution but also respects anatomical constraints. As qualitatively demonstrated in Fig. 2, this explicit supervision effectively suppresses spurious boundary artifacts, ensuring precise anatomical alignment with the ground truth.

IV. EXPERIMENTAL SETUP

A. Datasets and Preprocessing

1) ADNI Dataset: We use 10678 T1-weighted MRI scans from 1,920 subjects in the Alzheimer’s Disease Neuroimaging Initiative (ADNI) dataset¹, with 56.2% female, baseline ages of 54.9–94.6 years (mean: 74.3 years), and baseline diagnoses of 34.9% cognitively normal (CN), 55.1% mild cognitive impairment (MCI), and 10.1% AD. To construct longitudinal image pairs, we exhaustively pair all temporally ordered scans

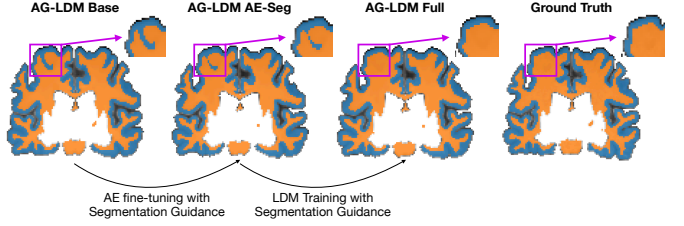


Fig. 2: Effect of segmentation-guided supervision: GM and WM segmentation of an MRI synthesized by AG-LDM Base, AG-LDM AE-Seg, and AG-LDM Full (conditioned on the same baseline MRI); Adding segmentation guidance at both stages produces segmentations closer to the ground truth.

within each subject. This yields 31,713 longitudinal pairs with mean scan interval of 2.89 years (median: 2.01 years, maximum: 15.92 years). We perform subject-level splitting in an 8:1:1 ratio: 25,498 pairs (1,534 subjects) for training, 3,129 pairs (194 subjects) for validation, and 3,086 pairs (192 subjects) for testing. No subject appears across multiple splits.

2) OASIS-3 External Validation: For external validation, we use the Open Access Series of Imaging Studies (OASIS-3)² dataset. The dataset comprises 573 subjects (41.5% female) with baseline ages of 43.0–92.0 years (mean: 66.9 years) and a bimodal diagnostic distribution (76.6% CN, 2.2% MCI, 21.2% AD). Following the same pairing strategy, we exhaustively pair all temporally ordered scans within each subject, yielding 1,965 pairs with mean scan interval of 4.57 years. After training on ADNI, the model is directly tested on OASIS-3 without fine-tuning, providing zero-shot generalization evaluation.

3) Preprocessing: All scans undergo standardized preprocessing: N4 bias-field correction [33], skull stripping [34], affine registration to MNI152 space, and resampling to 1.5mm isotropic resolution. Images are padded/cropped to $122 \times 146 \times 122$ voxels, with intensities clipped at 5th-99.5th percentiles and min-max normalized to $[0, 1]$.

B. Model Architecture

1) Autoencoder: We adopt the 3D variational autoencoder architecture from the MONAI Generative Models library [15], following the same configuration as BrLP [1]. The autoencoder uses a 3-channel latent representation with an encoder that progressively downsamples through four levels with channel dimensions (64, 128, 128, 128), using 2 residual blocks per level with group normalization (32 groups). The latent space achieves approximately $8 \times$ spatial downsampling. We initialize from publicly available pre-trained weights³ and fine-tune with anatomical supervision.

2) Segmentation Teacher: For anatomical supervision, we use an in-house 3D segmentation model based on the WarpSeg architecture⁴. WarpSeg is a semi-supervised, dual-decoder deep learning framework designed for data-efficient 3D brain MRI segmentation. The architecture features a shared encoder

²<https://www.oasis-brains.org>

³Pretrained Autoencoder is available at: <https://github.com/Project-MONAI/GenerativeModels>

⁴Our WarpSeg is available at: <https://github.com/WarpSeg>

that extracts multi-scale features, feeding into two distinct decoders: a coarse decoder that predicts six major tissue classes (background, GM, WM, ventricles, CSF, and deep gray matter) and a fine decoder that segments 30 detailed anatomical regions.

Only the output for the GM and WM is used for training. WarpSeg is pre-trained on a large-scale brain segmentation dataset and remains frozen during all training stages to provide consistent anatomical supervision without introducing additional trainable parameters.

3) Diffusion Model: The noise prediction network ϵ_θ adopts the MONAI 3D U-Net architecture [15], consistent with BrLP's implementation [1]. The network comprises three downsampling levels with channel dimensions (256, 512, 768). Self-attention mechanisms are applied at the two deepest resolutions using single-layer transformers. As described in Sec. III-D, the network processes 11 input channels through channel concatenation (Eq. 8). Each level uses 2 residual blocks with group normalization (32 groups).

C. Training and Inference

1) Training Configuration: Based on the performance on the ADNI validation set, we select optimal hyperparameters and training configurations for our model and comparison methods. Given that AG-LDM is designed from a simplified version of BrLP, we ensure that the overlapping hyperparameters between BrLP and AG-LDM are chosen to be the same.

Specifically, in the first stage as Sec. III-C, we fine-tune the pretrained autoencoder for 10 epochs using Adam optimizer with learning rate $\eta_{AE} = 5 \times 10^{-6}$ and effective batch size 16 (achieves via gradient accumulation from physical batch size 2). Adjusting from the hyperparameter setting in BrLP, we set KL divergence weight $\beta_{KL} = 1 \times 10^{-6}$, perceptual loss weight $\lambda_{perc} = 0.08$, adversarial loss weight $\lambda_{adv} = 0.1$, feature matching weight $\lambda_{fm} = 10$, and anatomical segmentation weight $\lambda_{seg} = 1.0$. The discriminator uses spectral normalization for training stability. We employ mixed precision training (FP16) with automatic mixed precision (AMP) to reduce memory consumption. This serves as the primary training configuration for our model in all experiments.

Following standard LDM training protocols [13], we apply a global latent space normalization to ensure unit variance. We compute a scale factor $s = 1/\text{Std}(\mathbf{z})$ from 1,000 randomly sampled training latents, scaling inputs by s before diffusion training and rescaling by $1/s$ during decoding.

In the second stage, we train the conditional LDM for 20 epochs using AdamW optimizer with learning rate $\eta_{LDM} = 2.5 \times 10^{-5}$ and batch size 8. The diffusion model follows DDPM [12] with $T = 1000$ training timesteps and a scaled linear noise schedule with $\beta_1 = 0.0015$ and $\beta_T = 0.0205$. Following Eq. 10, we augment the noise prediction objective with periodic anatomical supervision applied every $f_{seg} = 100$ iterations, using Dice loss weight $\gamma = 1 \times 10^{-5}$. For anatomical supervision during training, we perform fast 10-step DDIM sampling [14] from intermediate noisy states to obtain preliminary generated scans for segmentation comparison.

2) Inference and Evaluation: For any given scan pair from the ADNI testing split or the entire OASIS-3, the model generates the follow-up scan conditioned on the baseline scan and clinical covariates. We use DDIM [14] with 50 inference steps for efficient generation at test time. The generated follow-up scan is compared with the ground-truth follow-up scan by Mean Squared Error (MSE). Quality of the generated scans is measured by Peak Signal-to-Noise Ratio (PSNR). Beyond image quality, we also measure the anatomical accuracy of the generated scans. To do so, we segment both the generated scan and ground truth using SynthSeg [30] (FreeSurfer 7.4.1) and compute the volume for four clinically relevant ROIs that are also used for evaluation in BrLP: amygdala, hippocampus, lateral ventricles, and thalamus. Note that to make this evaluation independent from training, the post-hoc segmentation is based on SynthSeg, a different segmentor from WarpSeg used in training. The volumetric information of these brain ROIs is also not used for anatomical supervision during training. Lastly, we normalize these regional volumes by head size and calculate the absolute percentage error between predicted and ground-truth volumes, i.e. Brain-Region Volume MAE (%). Additionally, we report the WASABI score to assess global anatomical plausibility.

All experiments are conducted on a single NVIDIA H100 GPU (96GB). Training the autoencoder takes approximately 3 hours, and training the diffusion model takes approximately 8 hours. Inference takes about 1 second per sample.

V. RESULTS

A. Comparison with State-of-the-Art Methods

We compare **AG-LDM** against four state-of-the-art methods for longitudinal brain MRI progression modeling: 4D-DaniNet [5], Latent-SADM [8], CounterSynth [23], and BrLP [1]. Notably, BrLP serves as the representative state-of-the-art baseline for LDMs equipped with ControlNet conditioning and auxiliary progression modules. Table I summarizes image quality and anatomical precision for four selected ROIs on both the ADNI test set and OASIS-3 external validation.

On ADNI, **AG-LDM** achieves the best overall performance in 5 out of 7 metrics. It attains the best image quality (MSE/PSNR) and the lowest volumetric MAE in Amygdala and Hippocampus. While BrLP yields slightly lower errors in Lateral Ventricle and Thalamus (likely due to its auxiliary model explicitly optimizing these specific regional volumes) it suffers from a drastically higher WASABI score. This two-order-of-magnitude difference indicates that while BrLP may preserve specific regional volumes, it fails to maintain global morphometric plausibility. In contrast, AG-LDM minimizes both local ROI errors and global anatomical discrepancy, validating the effectiveness of our segmentation-guided strategy.

Figure 3 shows an example of the generated scan at 10-year follow-up for a randomly selected AD patient. While all methods generate visually appealing MRIs, AG-LDM generates brain structures more closely aligned with the ground truth. In contrast, BrLP and CounterSynth exhibit noticeably smaller lateral ventricles and enlarged thalamus regions in these slices, whereas AG-LDM accurately preserves the morphometry of these structures.

TABLE I: Quantitative comparison on Internal (ADNI) and External (OASIS-3) test sets. We report image fidelity, anatomical consistency, and brain-region volume MAE (%). WASABI measures anatomy-aware structural consistency, complementary to regional volume MAE. Regions of interest (ROIs) include Amyg. (Amygdala), Hippo. (Hippocampus), Lat. Vent. (Lateral Ventricle), Thal. (Thalamus). Best within each test set is in **bold**.

| Method | Internal Test Set (ADNI) | | | | | | | External Test Set (OASIS-3) | | | | | | |
|-------------------|--------------------------|--------------|--------------|--------------|-------------------------------|--------------|--------------|-----------------------------|--------------|--------------|--------------|-------------------------------|--------------|--------------|
| | Image Fidelity | | Anatomical | | Brain-Region Volume MAE (%) ↓ | | | Image Fidelity | | Anatomical | | Brain-Region Volume MAE (%) ↓ | | |
| | MSE ↓ | PSNR ↑ | WASABI ↓ | Amyg. | Hippo. | Lat. Vent. | Thal. | MSE ↓ | PSNR ↑ | WASABI ↓ | Amyg. | Hippo. | Lat. Vent. | Thal. |
| 4D-DaniNet [5] | 0.027 | 15.84 | 14.831 | 0.055 | 0.118 | 1.750 | 0.168 | 0.025 | 15.62 | 9.173 | 0.027 | 0.095 | 1.690 | 0.140 |
| Latent-SADM [8] | 0.022 | 16.59 | 2.591 | 0.030 | 0.073 | 1.434 | 0.117 | 0.023 | 16.34 | 4.839 | 0.029 | 0.065 | 1.308 | 0.089 |
| CounterSynth [23] | 0.005 | 23.19 | 3.658 | 0.016 | 0.028 | 0.308 | 0.039 | 0.004 | 24.28 | 1.834 | 0.013 | 0.024 | 0.380 | 0.049 |
| BrLP [1] | 0.006 | 22.16 | 8.250 | 0.028 | 0.044 | 0.190 | 0.035 | 0.005 | 22.91 | 7.311 | 0.031 | 0.060 | 0.773 | 0.056 |
| AG-LDM | 0.003 | 24.74 | 0.443 | 0.013 | 0.026 | 0.293 | 0.037 | 0.003 | 25.03 | 0.697 | 0.011 | 0.021 | 0.264 | 0.041 |

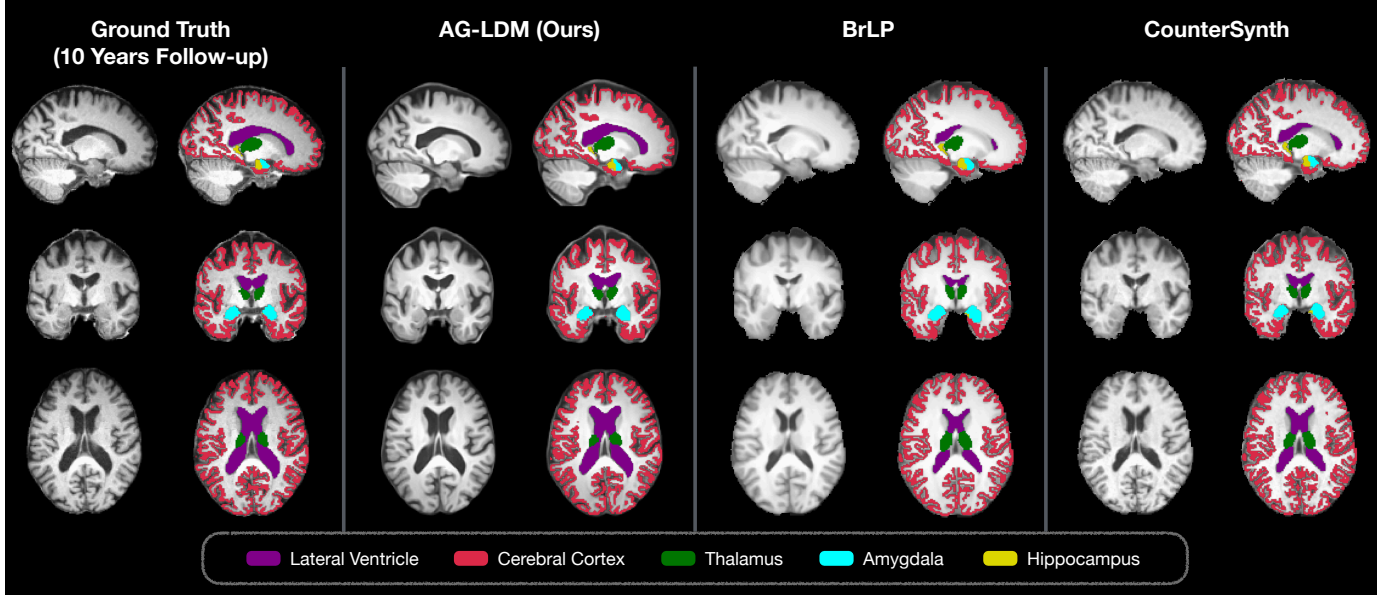


Fig. 3: Ten-year brain progression synthesis (73→83 years) for a randomly selected AD patient: Columns correspond to the ground truth follow-up scan and scans generated by AG-LDM, BrLP, and CounterSynth. For each method we show matched sagittal/coronal/axial slices with SynthSeg overlays (right image in each pair).

On the external OASIS-3 test set, AG-LDM demonstrates strong generalization capabilities (Table I). **AG-LDM** achieves comparable or even better image quality and anatomical precision metrics compared to ADNI. Notably, AG-LDM achieves 2-3× lower errors for all 4 ROIs and an order-of-magnitude improvement in WASABI score compared to BrLP, which shows substantially lower generalizability to the external dataset. The consistent performance of AG-LDM across both internal and external test sets validates the robustness of our combined normalization and anatomical supervision strategy.

B. Ablation Studies

Next, we inspect the influence of adding segmentation guidance to both stages of our model. We evaluate three distinct scenarios to isolate the impact of our contributions: removing segmentation supervision from both training stages (Base), which functions as a standard conditional LDM baseline (similar to vanilla DDIM) relying solely on reconstruction loss and channel-wise concatenation; applying segmentation guidance only during autoencoder fine-tuning (AE-Seg); and

incorporating anatomical supervision across both autoencoder and diffusion training stages (Full). To ensure our finding is not biased by the specific hyperparameter setting derived from the ADNI validation set, we train the autoencoder under 8 different hyperparameter configurations by varying learning rates ($\eta_{AE} \in \{10^{-7} \text{ to } 5 \times 10^{-5}\}$), feature matching weights ($\lambda_{fm} \in \{0, 1, 10\}$), perceptual loss weights ($\lambda_{perc} \in \{0.005 \text{ to } 0.08\}$), and KL divergence weights ($\beta_{KL} \in \{10^{-7} \text{ to } 5 \times 10^{-5}\}$). This yields 24 models (8 configurations × 3 variants). Crucially, all models use identical Stage 2 hyperparameters and global latent normalization, isolating the effect of anatomical supervision applied during autoencoder fine-tuning.

Figure 4 presents tissue-level anatomical consistency measured by Dice coefficient for two primary tissue types (WM and GM) and CSF across the entire brain, and Table II records volume MAE for the 4 ROIs similar to Table I. Results indicate progressive benefits of anatomical supervision. Starting from **Base**, adding segmentation guidance during autoencoder fine-tuning (**AE-Seg**) significantly improves tissue- and ROI-level anatomical consistency, particularly for CSF. Incorporat-

TABLE II: Ablation study on Internal (ADNI) and External (OASIS-3) test sets. Mean and standard deviation are computed over 8 hyperparameter configurations for each AG-LDM variant.

| Method | Internal (ADNI) – Volume MAE (%) ↓ | | | | External (OASIS-3) – Volume MAE (%) ↓ | | | |
|--------|------------------------------------|----------------------|----------------------|----------------------|---------------------------------------|----------------------|----------------------|----------------------|
| | Amyg. | Hippo. | Lat. Vent. | Thal. | Amyg. | Hippo. | Lat. Vent. | Thal. |
| AG-LDM | 0.042 ± 0.064 | 0.105 ± 0.152 | 0.763 ± 0.904 | 0.136 ± 0.266 | 0.040 ± 0.069 | 0.103 ± 0.168 | 0.635 ± 0.756 | 0.139 ± 0.279 |
| | 0.025 ± 0.018 | 0.067 ± 0.052 | 0.452 ± 0.144 | 0.076 ± 0.052 | 0.017 ± 0.009 | 0.050 ± 0.040 | 0.368 ± 0.114 | 0.084 ± 0.056 |
| | 0.022 ± 0.012 | 0.057 ± 0.050 | 0.411 ± 0.235 | 0.082 ± 0.051 | 0.016 ± 0.005 | 0.053 ± 0.047 | 0.353 ± 0.179 | 0.087 ± 0.054 |

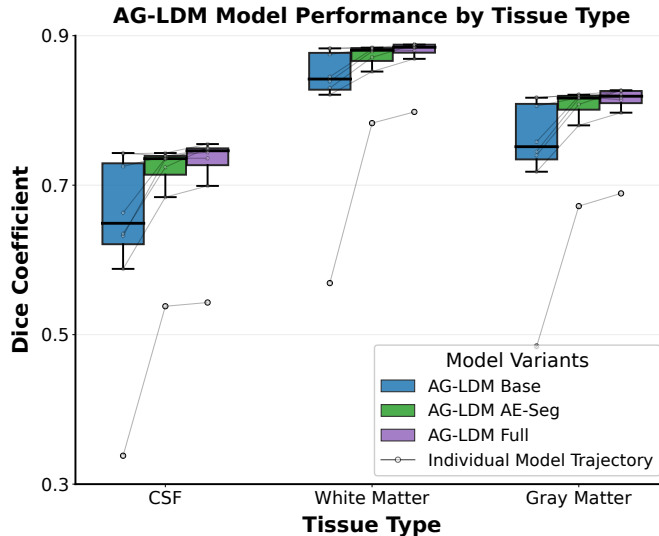


Fig. 4: Anatomical consistency measured by Dice coefficient for GM, WM, and CSF on the validation set. Each box represents 8 AG-LDM variants trained with different hyperparameter configurations.

ing periodic anatomical supervision during diffusion training (**Full**) yields additional gains for WM and GM preservation. The narrower boxplot distributions associated with the AG-LDM variants with segmentation guidance compared to the base model demonstrate that segmentation guidance not only improves performance but also stabilizes training, making the approach robust to hyperparameter choices.

C. Conditioning Effectiveness Analysis

Next, we evaluate how effectively our model utilizes conditional clinical covariates for brain MRI progression synthesis. The idea is that if the model does not learn conditional information, the conditional distribution degenerates to the marginal distribution, resulting in generated scans that are independent of the clinical covariates.

We randomly sample 50 subjects from the ADNI test set. For each subject, we generate follow-up predictions under different conditioning scenarios by selectively removing individual conditional inputs. When a condition is removed, we replace it with a neutral default value: continuous variables (starting age, follow-up age) are set to the dataset median, while categorical variables (sex, cognitive diagnosis) are set to zero. All other conditions remain at their true values. We then measure reconstruction quality using MSE between the generated and real follow-up images. The sensitivity to

TABLE III: Conditional Input Sensitivity Analysis: Percentage change (Mean ± SD) in reconstruction error (MSE) after replacing each conditional covariate to a non-informative null value. Larger positive values indicate greater sensitivity to conditional variables.

| Removed Variable | AG-LDM (Ours) | BrLP | Fold Diff. |
|---------------------|-----------------|---------------|--------------|
| Starting age | +408.3 ± 397.4% | +16.4 ± 42.8% | 24.9× |
| Follow-up age | +138.4 ± 189.1% | -4.4 ± 38.0% | 31.5× |
| Sex | +43.6 ± 149.7% | +11.9 ± 51.8% | 3.6× |
| Cognitive diagnosis | +36.2 ± 112.6% | +10.2 ± 50.1% | 3.5× |

each condition is quantified as the percentage change in MSE relative to the model using full clinical covariates: Sensitivity = $(MSE_{removed} - MSE_{full})/MSE_{full} \times 100\%$, where larger positive values indicate the model is more sensitive to the conditional covariates.

Given that BrLP represents the current state-of-the-art for brain MRI progression modeling, also supported by our previous experiments, and is the only publicly available baseline with comparable conditioning capabilities, we compare AG-LDM’s conditioning effectiveness against BrLP to quantify the practical benefits of our simplified architecture.

The results reveal a striking contrast in conditioning effectiveness between the two architectures (Table III). AG-LDM exhibits substantially higher sensitivity to conditional inputs, demonstrating 3.5–31.5× stronger reliance on clinical covariates compared to BrLP. Most dramatically, omitting the starting age condition in AG-LDM results in a 408% increase in MSE, and omitting follow-up age results in a 138% increase, while BrLP exhibits only 16% MSE change with respect to starting age and 4.4% MSE change to follow-up age. For sex and diagnosis information, AG-LDM demonstrates moderate but significant sensitivity (44% and 36% MSE change), while BrLP’s output remains largely unaffected (12% and 10%). These results confirm that direct channel-wise concatenation at the input level of LDM may be a more effective conditioning strategy than a segregated ControlNet.

D. Counterfactual Study

We assess whether the model captures normal aging and accelerated aging linked to AD through a counterfactual experiment on the ADNI testset. Specifically, we identify 200 pairs of longitudinal scans from subjects who remained cognitively normal (CN) at both timepoints, constraining that each pair has a time interval greater than 7 years to evaluate the model’s capacity for long-term progression synthesis. Using the baseline scan and the *actual follow-up age* as inputs, we

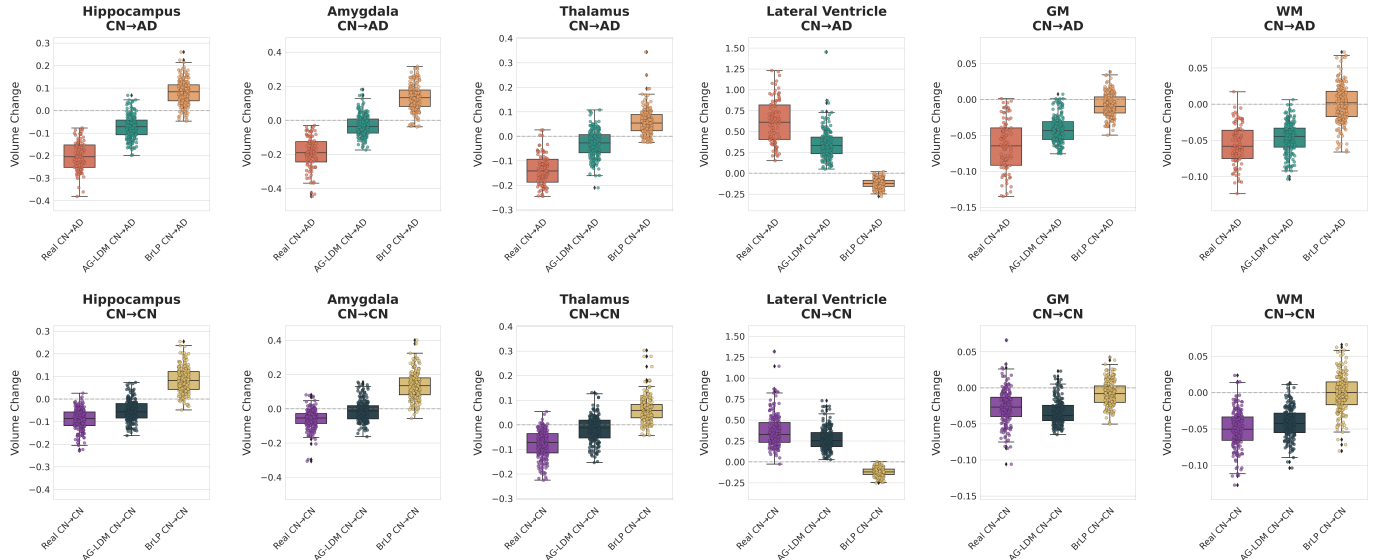


Fig. 5: Comparing Real and Synthesized Trajectories: Top row: comparing observed volume change among 200 real CN subjects with trajectories synthesized by AG-LDM and BrLP. Bottom row: comparing observed volume change among 200 real subjects converting from CN to AD with trajectories counterfactually synthesized by AG-LDM and BrLP. Each tile shows the relative volume change (ΔV_{rel}) in an ROI between the baseline and (real or synthesized) follow-up MRIs.

use AG-LDM to synthesize two future scans for each subject: 1) a *natural* trajectory conditioned on the diagnosis remaining CN (AG-LDM CN→CN), and 2) a *counterfactual* trajectory conditioned on the diagnosis converting to AD (AG-LDM CN→AD). For comparison, we also simulate the two future scans by BrLP. These synthesized trajectories are compared against the ground truth real longitudinal changes of the same 200 subjects (Real CN→CN) and, for reference, against a separate group of real ADNI subjects who converted from CN to AD (Real CN→AD, $n=93$).

We analyze real and synthesized trajectories of hippocampus, amygdala, thalamus, lateral ventricles, GM, and WM. All synthesized and real follow-up images are segmented with SynthSeg. For each subject and ROI, we compute head-size-normalized volumes and define the relative volume change as $\Delta V_{\text{rel}} = (V_{\text{follow-up}} - V_{\text{baseline}})/V_{\text{baseline}} \times 100\%$, where a positive ΔV_{rel} indicates volume expansion and a negative value indicates atrophy. Outliers are removed using an IQR rule. Figure 5 summarizes the distribution of ΔV_{rel} across real data, AG-LDM simulations, and BrLP simulations.

The real data exhibit expected biological patterns: mild atrophy during normal aging with moderate ventricular expansion, contrasting with sharper decline in AD, particularly in limbic regions (hippocampus and amygdala) alongside pronounced ventricular enlargement. AG-LDM approximates these signatures more closely than BrLP, aligning with the directionality of progression and preserving the relative ordering of effect sizes across ROIs (e.g., showing greater sensitivity in the hippocampus compared to the thalamus). For instance, under the counterfactual AD condition, AG-LDM correctly predicts hippocampus atrophy ($-7.3 \pm 5.0\%$), whereas BrLP erroneously predicts growth ($+8.1 \pm 5.4\%$). Similarly, for the **lateral ventricles**, while real AD subjects and AG-

LDM’s counterfactual prediction shows massive expansion ($+62.0 \pm 26.1\%$ and $+34.8 \pm 17.1\%$), BrLP predicts shrinkage ($-12.1 \pm 5.4\%$). Furthermore, AG-LDM successfully differentiates disease severity (e.g., hippocampus atrophy increases from -5.2% in natural aging to -7.3% in counterfactual AD), whereas BrLP produces nearly identical erroneous trajectories across conditions.

These results suggest that the conditioning mechanism in AG-LDM effectively steers synthesis along biologically plausible trajectories. The improved alignment between AG-LDM’s counterfactual simulations and observed longitudinal trends supports its potential utility for simulation and hypothesis testing in studies of brain aging and neurodegeneration.

VI. CONCLUSION

In this work, we presented AG-LDM, a streamlined latent diffusion framework for brain MRI progression modeling that prioritizes anatomical consistency through explicit segmentation guidance. By simplifying the conditioning mechanism and integrating a lightweight segmentation teacher, AG-LDM achieves state-of-the-art image quality and significantly reduces volumetric errors compared to complex multi-stage architectures. Our experiments demonstrate that AG-LDM effectively leverages clinical covariates to generate biologically plausible counterfactual trajectories, offering a reliable tool for visualizing individualized disease progression. While the current framework focuses on predicting specific follow-up scans, future work will extend AG-LDM to full longitudinal modeling, capturing complete temporal trajectories across multiple time points to provide a continuous and comprehensive view of neurodegenerative evolution.

REFERENCES

[1] L. Puglisi, D. C. Alexander, and D. Ravi, "Enhancing spatiotemporal disease progression models via latent diffusion and prior knowledge," in *International Conference on Medical Image Computing and Computer-Assisted Intervention*. Springer, 2024, pp. 173–183.

[2] A. L. Young, N. P. Oxtoby, S. Garbarino, N. C. Fox, F. Barkhof, J. M. Schott, and D. C. Alexander, "Data-driven modelling of neurodegenerative disease progression: thinking outside the black box," *Nature Reviews Neuroscience*, pp. 1–20, 2024.

[3] N. P. Oxtoby and D. C. Alexander, "Imaging plus x: multimodal models of neurodegenerative disease," *Current opinion in neurology*, vol. 30, no. 4, p. 371, 2017.

[4] A. L. Young, R. V. Marinescu, N. P. Oxtoby, M. Bocchetta, K. Yong, N. C. Firth, D. M. Cash, D. L. Thomas, K. M. Dick, J. Cardoso *et al.*, "Uncovering the heterogeneity and temporal complexity of neurodegenerative diseases with subtype and stage inference," *Nature communications*, vol. 9, no. 1, p. 4273, 2018.

[5] D. Ravi, S. B. Blumberg, S. Ingala, F. Barkhof, D. C. Alexander, N. P. Oxtoby, A. D. N. Initiative *et al.*, "Degenerative adversarial neuroimage nets for brain scan simulations: Application in ageing and dementia," *Medical Image Analysis*, vol. 75, p. 102257, 2022.

[6] T. Xia, A. Chartsias, C. Wang, S. A. Tsaftaris, A. D. N. Initiative *et al.*, "Learning to synthesise the ageing brain without longitudinal data," *Medical Image Analysis*, vol. 73, p. 102169, 2021.

[7] R. He, G. Ang, D. Tward, and A. D. N. Initiative, "Individualized multi-horizon mri trajectory prediction for alzheimer's disease," in *International Conference on Medical Image Computing and Computer-Assisted Intervention*. Springer, 2024, pp. 26–37.

[8] J. S. Yoon, C. Zhang, H.-I. Suk, J. Guo, and X. Li, "Sadm: Sequence-aware diffusion model for longitudinal medical image generation," in *International Conference on Information Processing in Medical Imaging*. Springer, 2023, pp. 388–400.

[9] M. Litrico, F. Guarnera, M. V. Giuffrida, D. Ravì, and S. Battiatto, "Tadm: Temporally-aware diffusion model for neurodegenerative progression on brain mri," in *International Conference on Medical Image Computing and Computer-Assisted Intervention*. Springer, 2024, pp. 444–453.

[10] W. Peng, T. Bosschieter, J. Ouyang, R. Paul, E. V. Sullivan, A. Pfefferbaum, E. Adeli, Q. Zhao, and K. M. Pohl, "Metadata-conditioned generative models to synthesize anatomically-plausible 3d brain mris," *Medical Image Analysis*, vol. 98, p. 103325, 2024.

[11] B. Jafrahesteh, W. Peng, C. Wan, Y. Luo, E. Adeli, and Q. Zhao, "Wasabi: A metric for evaluating morphometric plausibility of synthetic brain mrис," in *International Conference on Medical Image Computing and Computer-Assisted Intervention*. Springer, 2025, pp. 684–694.

[12] J. Ho, A. Jain, and P. Abbeel, "Denoising diffusion probabilistic models," *Advances in neural information processing systems*, vol. 33, pp. 6840–6851, 2020.

[13] R. Rombach, A. Blattmann, D. Lorenz, P. Esser, and B. Ommer, "High-resolution image synthesis with latent diffusion models," in *Proceedings of the IEEE/CVF conference on computer vision and pattern recognition*, 2022, pp. 10684–10695.

[14] J. Song, C. Meng, and S. Ermon, "Denoising diffusion implicit models," *arXiv preprint arXiv:2010.02502*, 2020.

[15] W. H. Pinaya, P.-D. Tudosiu, J. Dafflon, P. F. Da Costa, V. Fernandez, P. Nachev, S. Ourselin, and M. J. Cardoso, "Brain imaging generation with latent diffusion models," in *MICCAI Workshop on Deep Generative Models*. Springer, 2022, pp. 117–126.

[16] G. Kwon, C. Han, and D.-s. Kim, "Generation of 3d brain mri using auto-encoding generative adversarial networks," in *International Conference on Medical Image Computing and Computer-Assisted Intervention*. Springer, 2019, pp. 118–126.

[17] S. Xing, H. Sinha, and S. J. Hwang, "Cycle consistent embedding of 3d brains with auto-encoding generative adversarial networks," in *Medical Imaging with Deep Learning*, 2021.

[18] Z. Dorjsembe, S. Odonchimed, and F. Xiao, "Three-dimensional medical image synthesis with denoising diffusion probabilistic models," in *Medical imaging with deep learning*, 2022.

[19] K. Han, Y. Xiong, C. You, P. Khosravi, S. Sun, X. Yan, J. S. Duncan, and X. Xie, "Medgen3d: A deep generative framework for paired 3d image and mask generation," in *International Conference on Medical Image Computing and Computer-Assisted Intervention*. Springer, 2023, pp. 759–769.

[20] W. Peng, E. Adeli, T. Bosschieter, S. H. Park, Q. Zhao, and K. M. Pohl, "Generating realistic brain mris via a conditional diffusion probabilistic model," in *International conference on medical image computing and computer-assisted intervention*. Springer, 2023, pp. 14–24.

[21] S. Lüpke, Y. Yeganeh, E. Adeli, N. Navab, and A. Farshad, "Physics-informed latent diffusion for multimodal brain mri synthesis," in *International Conference on Medical Image Computing and Computer-Assisted Intervention*. Springer, 2024, pp. 198–207.

[22] R. Yesiloglu, W. Peng, M. T. Islam, and E. Adeli, "Neural autoregressive modeling of brain aging," in *MICCAI Workshop on Deep Generative Models*. Springer, 2025, pp. 341–350.

[23] G. Pombo, R. Gray, M. J. Cardoso, S. Ourselin, G. Rees, J. Ashburner, and P. Nachev, "Equitable modelling of brain imaging by counterfactual augmentation with morphologically constrained 3d deep generative models," *Medical Image Analysis*, vol. 84, p. 102723, 2023.

[24] F. Huang, A. Wang, B. Li, B. Trang, R. Yesiloglu, T. Hua, W. Peng, and E. Adeli, "Cycle diffusion model for counterfactual image generation," in *International Workshop on PRedictive Intelligence In MEdicine*. Springer, 2025, pp. 173–185.

[25] Y. Yeganeh, A. Farshad, I. Charisiadis, M. Hasny, M. Hartenberger, B. Ommer, N. Navab, and E. Adeli, "Latent drifting in diffusion models for counterfactual medical image synthesis," in *Proceedings of the Computer Vision and Pattern Recognition Conference*, 2025, pp. 7685–7695.

[26] A. Q. Wang, F. Huang, B. Trang, W. Peng, M. Abbasi, K. Pohl, M. R. Sabuncu, and E. Adeli, "Generating novel brain morphology by deforming learned templates," in *International Conference on Medical Image Computing and Computer-Assisted Intervention*. Springer, 2025, pp. 207–217.

[27] M. Wilms, J. J. Bannister, P. Mouches, M. E. MacDonald, D. Rajashekhar, S. Langner, and N. D. Forkert, "Invertible modeling of bidirectional relationships in neuroimaging with normalizing flows: application to brain aging," *IEEE Transactions on Medical Imaging*, vol. 41, no. 9, pp. 2331–2347, 2022.

[28] N. Wu, N. Jayakumar, J. Xing, and M. Zhang, "Igg: Image generation informed by geodesic dynamics in deformation spaces," in *International Conference on Information Processing in Medical Imaging*. Springer, 2025, pp. 232–246.

[29] V. Fernandez, W. H. L. Pinaya, P. Borges, M. S. Graham, P.-D. Tudosiu, T. Vercauteren, and M. J. Cardoso, "Generating multi-pathological and multi-modal images and labels for brain mri," *Medical Image Analysis*, vol. 97, p. 103278, 2024.

[30] B. Billot, D. N. Greve, O. Puonti, A. Thielscher, K. Van Leemput, B. Fischl, A. V. Dalca, J. E. Iglesias *et al.*, "Synthseg: Segmentation of brain mri scans of any contrast and resolution without retraining," *Medical image analysis*, vol. 86, p. 102789, 2023.

[31] L. Henschel, S. Conjeti, S. Estrada, K. Diers, B. Fischl, and M. Reuter, "Fastsurfer-a fast and accurate deep learning based neuroimaging pipeline," *NeuroImage*, vol. 219, p. 117012, 2020.

[32] B. Jafrahesteh, "WarpSeg: Lightweight 3d tissue segmentation model," <https://github.com/BahramJafrahesteh/WarpSeg>, 2025, accessed: Nov. 2025.

[33] N. J. Tustison, B. B. Avants, P. A. Cook, Y. Zheng, A. Egan, P. A. Yushkevich, and J. C. Gee, "N4itk: improved n3 bias correction," *IEEE transactions on medical imaging*, vol. 29, no. 6, pp. 1310–1320, 2010.

[34] A. Hoopes, J. S. Mora, A. V. Dalca, B. Fischl, and M. Hoffmann, "Synthstrip: Skull-stripping for any brain image," *NeuroImage*, vol. 260, p. 119474, 2022.